united nations
educational, scientific
and cultural
organization

international atomic
energy agency

the
abdus salam
international centre for theoretical physics

School on "Exploring the Atmosphere by Remote Sensing Techniques"
18 October - 5 November 1999

1151-15

"Studying Atmospheric Aerosols by LIDAR"

G.-P. Gobbi
IFA/CNR
Rome
Italy

School on "EXPLORING THE ATMOSPHERE BY REMOTE-SENSING TECHNIQUES"
International Centre for Theoretical Physics – Trieste, October 1999

STUDYING ATMOSPHERIC AEROSOLS BY LIDAR

Gian Paolo Gobbi

Istituto di Fisica dell'Atmosfera CNR – Rome –ITALY
(gobbi@lux.ifa.rm.cnr.it)

Layout of the lectures:

School on "EXPLORING THE ATMOSPHERE BY REMOTE-SENSING TECHNIQUES"
International Centre for Theoretical Physics – Trieste, October 1999

STUDYING ATMOSPHERIC AEROSOLS BY LIDAR

Gian Paolo Gobbi
(gobbi@ifa.rm.cnr.it)
Istituto di Fisica dell'Atmosfera CNR
Rome - ITALY

Lidars operate by sending laser pulses into the atmosphere and collecting the backscattered light by means of telescopes provided with highly sensitive photodetectors.

Analysis of the signal intensity then allows a range-resolved inference of the physical and chemical properties of the scattering media (S).

Principal components of a lidar system:

Emitter: Pulsed lasers (from UV to IR). Nd-YAG, Ruby, Alexandrite, Ti-Sa, Diode, etc.;

Receiver: Optical telescopes. From single lens (0.01 m^2) to multiple-mirror (10 m^2);

Bandpass: Interference filters ($\Delta\lambda$ 0.1-10 nm), monocromators, interferometers, etc.;

Detector: Photomultipliers (UV-NIR), Avalanche photodiodes (IR) (10^5-10^7 current gain);

Signal acquisition: A/D conversion, Photon counting (10-100 Mhz sampling rate or bandpass capability); (S)

Typical laser beam divergence of 1 mrad generates spots of 1 m at 1 km and of 10 m at 10 km.

Considering that typical range resolution is 10-100 m the resulting lidar sampling volume is very small;

High laser repetition rates (10-100 Hz) allow for short term averaging (seconds);

These characteristics allow to study atmospheric processes ranging from the micro to the macro scale.

Similarly to radars, the return time of the laser pulse (dt) indicates the distance (R) of the scattering object: $R = c\ dt/2$

Typical laser wavelengths of the order of one micron (0.001 mm), permit good detection of objects of similar size. In fact, elastic backscattering is quite efficient in this case

Therefore, lidars are ideal instruments to remotely observe aerosol and thin clouds, which are made of particles of size ranging between hundredths and tens of microns.

Lidars also detect atmospheric gases.

In fact:

- Rayleigh scattering allows for good definition of the atmospheric molecular density (and consequently temperature) up to z≈100 km; (S T)
- Differential absorbtion allows for detection of trace gases as Ozone, Water vapor, Sulfur dioxide etc. at several kilometers from the system; (S dial)
- Raman scattering allows for definition of atmospheric density, temperature and of trace gases concentration (H_2O, SO_2, CO_2, etc.) (S raman)

This series of lectures shall focus onto the lidar detection of aerosols and clouds.

The scientific interest in the study of these two atmospheric constituents is due to their role in controlling the planet climate.

In fact, one of the global effects of clouds is to cool the planet by reflecting back to space part of the incoming solar radiation. Overall, aerosol too reflect solar radiation. It is estimated that the cooling effect of aerosols is approximately 1/30th of the cloud-induced one. Since the atmospheric burden of anthropogenic aerosols is steadily growing, their radiative and cloud-modifing effects keep growing too.

Volcanic aerosols too tend to cool the planet. These particles form in the stratosphere following gas and particle injection by major eruptions.
Due to its vertical stability, volcanic aerosols remain in the stratosphere for years, producing a global, long lasting cooling of some tenths of a degree.

One of the major unknowns about atmospheric aerosols is their altitude distribution. Lidars represent the best way to reduce such uncertainty.

The Lidar Equation:

$$E(\lambda, R) = E_L \bullet (c\,\tau_d/2) \bullet (A_0/R^2) \bullet \xi(\lambda) \bullet \beta(\lambda, R) \bullet T^2(R)$$

...describes the amount of energy reaching the lidar detector from the distance R, and during the integration time interval τ_d, which in turn defines the lidar profile range resolution: $dR = c\,\tau_d / 2$

- E_L : Laser pulse energy;
- R : Range;
- A_0 : Area of lidar receiver (telescope);
- $\xi(\lambda)$: Receiver spectral transmission;
- c : Speed of light;
- $\beta(\lambda, R)$: Volume backscatter coefficient;
- $T(\lambda, R)$: Atmospheric transmittance

The two variables carrying the geophysical information we want to retrieve are: $\beta(\lambda, R)$: the volume backscatter coefficient, and $T(\lambda, R)$, the Atmospheric transmittance

The volume backscatter coefficient of a species x being:

$$\beta_x(\lambda, R) = N_x(R) \bullet d\sigma_{\pi x}(\lambda, \theta) / d\Omega$$

where N_x and $d\sigma_{\pi x}(\lambda, \theta) / d\Omega$ represent the volume number concentration and the differential scattering cross section (at $\theta = 180^0$), respectively.

In the case of elastic backscatter from the atmosphere, $\beta(\lambda, R)$ can be expressed as:

$$\beta_{m+a}(\lambda, R) = \beta_m(\lambda, R) + \beta_a(\lambda, R)$$

where the subscripts "m" and "a" stand for the molecular and the aerosol (particulate) component, respectively. In fact, an aerosol-free atmosphere is only found above an altitude of about 30 km.

The atmospheric transmittance between the lidar site (R=0) and the range R can be expressed as:

$$T(\lambda, R) = e^{-\int_0^R \sigma(\lambda, R)\,dR}$$

Where $\sigma(\lambda, R)$ is the atmospheric extinction coefficient:

$$\sigma_x(\lambda, R) = N_x(R)\,\sigma_{xs}(\lambda)$$

with $\sigma_{xs}(\lambda)$ the species extinction cross section.

Again, in an atmosphere composed of molecules and aerosols we can express σ as:

$$\sigma_{m+a}(\lambda, R) = \sigma_m(\lambda, R) + \sigma_a(\lambda, R)$$

Solving the lidar equation:

By omitting the range and wavelength-dependence symbols and assuming the receiver spectral transmittance to be $\xi(\lambda)=1$ we obtain:

$$E = E_L \cdot \frac{c\tau_d}{2} \cdot \frac{A_0}{R^2} \cdot (\beta_m + \beta_a) \cdot e^{-2\int_0^R (\sigma_m + \sigma_a)\,dR}$$

This equation contains the two unknowns β_a and σ_a (β_m and σ_m are either measured or modeled). To be solved it needs some relationship linking the two variables. Collis and Russell (1976) indicated as a general approximation the following one:

$$\beta_a = \text{cost}\ \sigma_a^g$$

with g depending on the specific properties of the scattering medium and generally spanning the range $0.67<g<1$. Several versions of this relationship have been used in literature (Klett, 1985; Kovalev, 1993)

Klett (1985) showed that a good retrieval of backscatter from the lidar measurement can only be obtained if a functional relationship, $\beta_a = f(\sigma_a)$, not a fixed one, is employed. We shall see later how the relationship between β and σ can be determined.

One of the most popular solutions of the lidar equation is the analytical one described by Klett (1985):

$$\beta_a(R)+\beta_m(R)=\frac{\exp(S'-S_c')}{\left[\frac{1}{\beta_c}+2\int_R^{R_c}\frac{\exp(S'-S_c')dR}{B_a}\right]}$$

This is a stable solution, however, it contains the functional relationship $B_a = f(\sigma_a) = \beta_a / \sigma_a$, which forces an iterative process to retrieve the correct value of β_a. (β_m is derived either from air density measurements or models).

This solution has been found by defining the range corrected signal:

$$S(R)=\ln\left[E(R)\cdot R^2/\tau_d\right]$$

which converts the lidar equation into:

$$\frac{dS}{dR}=\frac{1}{\beta_{a+m}}\frac{d\beta_{a+m}}{dR}-2\sigma_{a+m}=\frac{1}{\beta_{a+m}}\frac{d\beta_{a+m}}{dR}-\frac{2\beta_{a+m}}{B_a}+2\beta_m\left(B_a^{-1}-B_m^{-1}\right)$$

By defining now the new signal variable S':

$$S'-S_c'=S-S_c+\frac{2}{B_m}\int_R^{R_c}\beta_m dR'-2\int_R^{R_c}\frac{\beta_a}{B_a}dR'$$

the latter becomes:

$$\frac{dS'}{dR}=\frac{1}{\beta_{a+m}}\frac{d\beta_{a+m}}{dR}-\frac{2\beta_{a+m}}{B_a}$$

which is solved by the Klett equation after definition of the boundary values at $R=R_m$, the calibration range ($R< R_c$).

A few useful formulas about cross sections:

The differential backscatter cross section of the "average" air molecule (below 100 km) [Hinkley, 1976]:

$$d\sigma_m(\lambda,\pi)/d\Omega = 5.45\,[\lambda(\mu m)/0.55]^{-4}\times 10^{-28}\ cm^2\ sr^{-1}$$

Notice the characteristic λ^{-4} dependance of the scattering.
At sea level (typical molecular density $N_m = 2.5\times10^{19}\ cm^{-3}$) this leads to:

$$\beta_m(\lambda,0) = [\lambda(\mu m)/0.55]^{-4}\times 1.39\times10^{-6}\ cm^{-1}\ sr^{-1}$$

From the Rayleigh scattering theory, the extinction/backscatter ratio of air molecules is:

$$\sigma_m/\beta_m = 4\pi/1.5 = 8.378$$

(S cross sect)

Backscattering from particles:

The Mie theory is the most common tool employed to compute scattering properties of atmospheric particles. It describes the scattering of spherical particles with size comparable to the incident wavelength. It applies well to liquid aerosols, cloud and fog droplets. It has drawbacks in the case of solid (dust, smoke) aerosols and ice crystals.

The Mie backscatter coefficient of a size distribution $N_a(r)$ of spherical particles is:

$$\beta_a(\lambda)=\int_0^{\infty}\sigma_\beta(r,\lambda,m)\cdot N_a(r)dr$$

where σ_β is the Mie backscatter cross section, and r and $m=n-ik$ represent the particle's radius and complex refractive index, respectively.

In the following sections these properties will be described in detail.

The "Mie" backscatter cross section $\sigma_\beta(r, \lambda, m)$ can be written as:

$$\sigma_\beta(r,\lambda,m) = \pi r^2 Q_\beta(x,m)$$

where $Q_\beta(x, m)$ is the backscatter efficiency, provided as a solution of e.m. scattering by Mie(e.g. Kerker [1969]). $Q_\beta(x, m)$ is a complex function of particles refractive index and of the "Mie" parameter:

$$x = 2\pi r/\lambda$$

In a similar fashion, the "Mie" extinction cross section $\sigma_\varepsilon(r, \lambda, m)$ can be written:

$$\sigma_\varepsilon(r,\lambda,m) = \pi r^2 Q_\varepsilon(x,m)$$

where $Q_\varepsilon(x, m)$ is the extinction efficiency. Q_β and Q_ε are expressed by an infinite series of Riccati-Bessel functions of x and mx. Some examples of the dependence of Q_β on x and mx are reported *hereafter* (S):

To compute backscatter and/or extinction coefficients of a distribution of particles N(r) (cm^{-3}) the product $\sigma_\beta N(r)$ ($cm^2\ sr^{-1}\ cm^{-3} = cm^{-1}\ sr^{-1}$) must be integrated over r:

$$\beta_a=\int_0^{\infty}Q_\beta\pi r^2N(r)dr$$

One of the most popular analytical formulations of size distributions is the log-normal one:

$$N(r)=\frac{dN}{d\log r}=\frac{N}{\sqrt{2\pi}\log\sigma}\exp\left[-\frac{(\log r-\log r_m)^2}{2\log^2\sigma}\right]$$

where r_m and σ *stand for* the distribution modal radius and width, respectively. This function has been shown to reproduce pretty well the bell-shaped dispersion of natural aerosols.

The build-up of aerosols backscatter can then be illustrated by the following (S):

Backscatter and depolarization ratio

A common way to present lidar data (and avoid dealing with the several orders of magnitude range of lidar signals) is the backscatter ratio:

$$R_B = (\beta_a + \beta_m) / \beta_m$$

Laser light is often polarized. Polarization results to be an useful tool to investigate aerosol phase (liquid vs. solid, i.e., droplets vs. crystals): in fact, spheres do not introduce any depolarization when backscattering a polarized beam. Conversely, non-spherical particles depolarize part of the incident polarized light they backscatter.

The common way to quantify depolarization of lidar signals is the depolarization ratio:

$$D = S_\perp / S_\parallel$$

where $S_\perp$ and $S_\parallel$ represent the lidar signal detected on polarization planes perpendicular and parallel to the laser one, respectively.

Therefore, polarization lidars need to operate two detection channels.

Depolarization induced by air molecules does not exceed 1%. This is theoretically quantified and explained as due to their non-symmetrical structure [Young, 1980].

A theoretical description of lidar depolarization from particles of size comparable to the wavelength is still rather qualitative. In fact, analytical solutions are obtained only for particles with an axis of symmetry, i.e., rather regular ones, e.g., Toon et al., [1990], Mishchenko et al., [1997]. (S)

Actual observations show a consistent "saturation" in the depolarization at D~50%, generated by simple solid particles (ice crystals, desert dust). (S)

Such behavior allows for inference of the aerosol phase (S)

Aerosols and climate

As previously mentioned, the scientific interest in the study of aerosols is due to their role in controlling the planet climate. In fact, aerosols scatter and absorb solar radiation and provide cloud condensation sites. The model-simulated effects of aerosols on climate tend to counterbalance green-house warming [e.g., Charlson, 1995] (P)

However, some indetermination still exists on the sign of the effects (warming or cooling) of absorbing particles as desert dust. We need to remember that desert dust is the second contributor (after marine) to the global aerosol load. (P)

Radiative effects of desert dust strongly depend on aerosol altitude, a poorly known parameter [Liao, 1998].

This situation explains the interest in studying desert dust and marine aerosol by lidar.

The extinction/backscatter relationship for desert dust and marine aerosols:

To quantitatively invert the lidar signal a model has been developed to explore and parameterize this extinction/backscatter relationship R_{ea}.

The approach of this model is simple [Gobbi, 1998] (KSL):

1) look at the variability of R_{ea} observed in nature;
2) determine dispersion and behavior of these relationships;
3) fit the resulting data by analytical curves (usually polynomials in log-log coordinates);

SOME CONCLUSIONS:

LIDARS provide an efficient technique to observe atmospheric minor constituents with high spatial and temporal resolution;

Remote-sensing of the atmosphere necessitates the synergic contribution of active and passive techniques, operating both from space and from the ground;

During the next century LIDAR applications will conquer a large share of the global remote sensing activities;

Analysis of processes observed by lidar is still an open field, deserving the attention of good scientists.

REFERENCES:

A list of over 800 lidar-related papers can be found at the www site:
http://www.sm.org/HOMES/GENERAL/BIBLIO/biblio97.htm

Charlson, R. J. (Ed.) Aerosol forcing of climate, J. Wiley, 416pp, New York, 1995.

d'Almeida, G., P. Koepke, and E. P. Shettle, Atmospheric aerosols, 561 pp., A Deepak, Hampton, VA, 1991.

Gobbi, G. P., Parameterization of atmospheric aerosol physical properties on the basis of Nd:YAG lidar observations, Applied Optics, 37, 4713-4720, 1998.

Hinkley, E. D. (Ed.), Laser monitoring of the atmosphere, Springer Verlag, 300pp, New York, 1976.

Kerker, M., The scattering of light and other electromagnetic radiation, Acad. Press, New York, 1969

Klett, J. D., Lidar inversion with variable backscatter/extinction ratios, Applied Optics, 24, 1638-1643, 1985.

Kovalev, V. A., Lidar measurement of the vertical aerosol extinction profiles with range-dependent backscatter to extinction ratio, Applied Optics, 30, 6053-6065, 1983.

Liao, H., and J.H. Seinfeld, Radiative forcing by mineral dust aerosols: Sensitivity to key variables, J. Geophys. Res., 103, 31637-31645, 1998.

Measures, R. M., Laser Remote Sensing, J. Wiley, New York, 510 pp., 1984.

Mishchenko, M. I. et al., Modelling phase functions for dustlike tropospheric aerosols using a shape mixture of randomly oriented polydisperse spheroids, J. Geophys. Res., 102, 16,831-16,847, 1997.

Toon, O. B., E. V. Browell, S. Kinne and J. Jordan, An analysis of lidar observations of polar stratospheric clouds, Geophys. Res. Lett., 17, 393-396, 1990.

Young, A. T., Revised depolarization corrections for atmospheric extinction, Appl. Opt., 19, 3247-3248, 1980.

Lidar-related Web Sites:

LIDAR BIBLIOGRAPHY:	http://www.sm.org/HOMES/GENERAL/BIBLIO/biblio97.htm
LIDAR DIRECTORY:	http://www-arb.larc.nasa.gov/lidar/directory.html
Shuttle lidar LITE:	http://www-arb.larc.nasa.gov/lite/

MEASURES, 1984

TABLE 6.1. OPTICAL INTERACTIONS OF RELEVANCE TO LASER ENVIRONMENTAL SENSING

Technique	Physical description
Rayleigh scattering	laser radiation elastically scattered from atoms or molecules is observed with no change of frequency 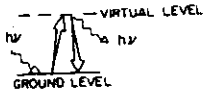
Mie scattering	laser radiation elastically scattered from small particulates or aerosols (of size comparable to wavelength of radiation) is observed with no change in frequency 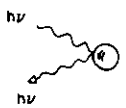
Raman scattering	laser radiation inelastically scattered from molecules is observed with a frequency shift characteristic of the molecule ($h\nu - h\nu^* = E$) 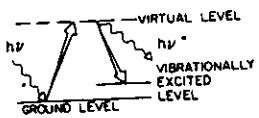
Resonance scattering	laser radiation matched in frequency to that of a specific atomic transition is scattered by a large cross section and observed with no change in frequency 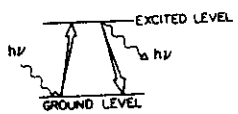
Fluorescence	laser radiation matched to a specific electronic transition of atom or molecule suffers absorption and subsequent emission at lower frequency; collision quenching can reduce effective cross section of this process; broadband emission is observed with molecules 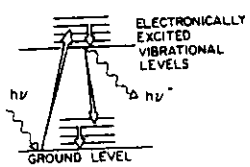

TABLE 6.1 (*Continued*)

Technique	Physical description
Absorption	observe attenuation of laser beam when frequency matched to the absorption band of given molecule 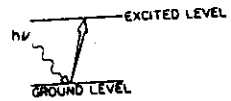
Differential absorption and scattering (DAS)	the differential attenuation of two laser beams is evaluated from their backscattered signals when the frequency of one beam is closely matched to a given molecular transition while the other's frequency is somewhat detuned from the transition 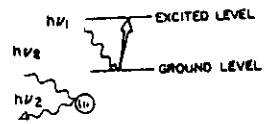

sections observed for each process is schematically presented in Fig. 6.1. It is evident from this figure that the cross section for Mie scattering can be so large that just a few appropriate-size scatters could give rise to a scattered signal that would completely swamp any Rayleigh- or Raman-scattered component. This implies that quite low concentrations (or changes in concentration) of dust or aerosols can be detected.

Although resonance scattering, sometimes referred to as atomic or resonance fluorescence, also has an inherently large cross section, collision quenching with the more abundant atmospheric species generally ensures that the detected signal is small; consequently this technique is used to best effect in studies of the trace constituents in the upper atmosphere (Hake et al., 1972; Gibson and Sandford, 1972, 1971; Aruga et al., 1974; Felix et al., 1973). The influence of collision quenching on molecular fluorescence can be equally detrimental, particularly where long-lived states are involved (Measures and Pilon, 1972). The broadband nature of molecular fluorescence invariably leads to a low value for the signal-to-noise ratio where background radiation forms the major component of noise (Wang, 1974; Byer, 1975). In the event that the fluorescence is long-lived, the spatial resolution can be degraded.

As we have seen earlier (Section 3.5.2), Raman scattering is an inelastic scattering process wherein the laser radiation may be thought of as raising the molecule to a virtual level from which it immediately decays (in $< 10^{-14}$ s), with the subsequent emission of radiation having a different wavelength. The difference in energy between the incident and emitted photons is a characteris-

TABLE 5.2. TYPES OF LASERS RELEVANT TO REMOTE SENSING

	Solid State	Gas	Liquid	Semiconductor
Representative examples	Ruby Neodymium (YAG) Alexandrite	XeCl (rare-gas halide) N_2 (transient) $HgBr_2/HgBr$ (dissociation) CO_2 (molecular)	Organic dyes such as: Rhodamine 6G Coumarin Cresyl violet	GaAs GaAsP InAs $Pb_{1-x}Sn_xSe$
Primary pumping technique	Flashlamp	Intense electrical discharge in gas	Flashlamp or laser	High current injection leading to n, p radiative annihilation at an n–p junction
Range of wavelengths and tuning	Ruby (694.3 nm)—thermal tuning ±0.4 nm Nd–YAG (1.06 μm) Alexandrite—tunable (701–818 nm) Second (or third) harmonic generation possible with all three kinds	H_2 (116, 160 nm) Xe_2 (170 nm) KrF (249 nm) XeCl (308 nm) N_2 (337 nm) $HgBr_2/HgBr$ (502–504 nm) DF or HF (2.7–4.0 μm) CO (5.0–5.7 μm) CO_2 (9.0–11 μm) HCN (337 μm)	Large range of dyes provide wavelengths from 340 nm to 1.1 μm Typical tuning range per dye ≈ 40 nm with widths of 0.1–0.01 nm possible with grating or prism (+ etalon) arrangement	$GaAsP–Pb_{1-x}Sn_xSe$ (550 nm to 32 μm) Tuning possible by changing current, applying pressure or magnetic field
Modes of operation and pulse duration	Q-switching leads to 10–100-ns pulses Mode-locking can yield 10-ps pulses	Fast discharges lead to pulses that typically range from 1 ns to 1 μs Q-switching possible with certain molecular gas lasers, cavity dumping with others	When N_2 laser pumped pulses are ~ 5–10-ns When flashlamp pumped 0.3–1-μs pulses Cavity dumping of latter can yield 30-ns pulses	Current pulsed but requires cooling and efficient heat sink 10 ns to 1μs possible
Peak power and energy/pulse attainable	For ruby and Nd–YAG 10^6–10^8 W and 1–10 J when Q-switched; for Alexandrite lasers 10^7 W and 500 mJ	10^4–10^7 W and 1 mJ to 1 J	10^4–10^6 W in narrow, tunable bandwidth; 0.1–3 J	100 W possible from laser diode arrays

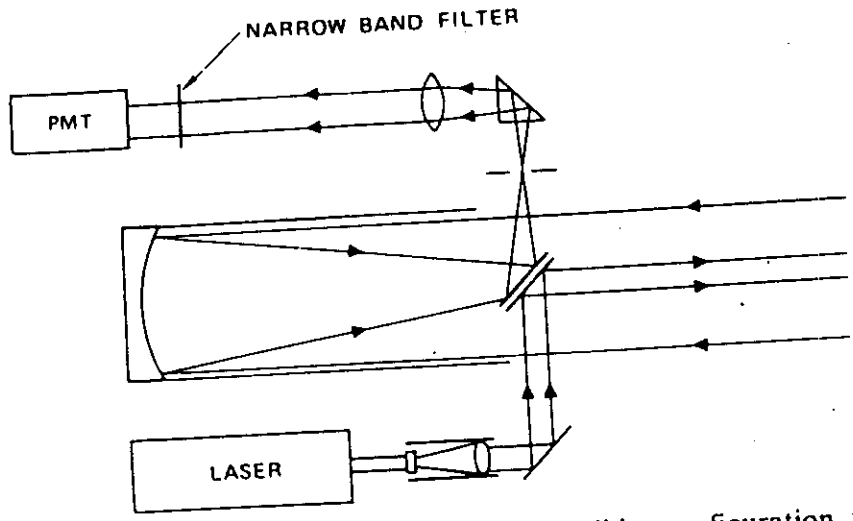

Fig. 4.1. Schematic diagram of fundamental lidar configuration, with coaxial transmitter/receiver geometry

Differential Absorption Lidar (DIAL) Concept

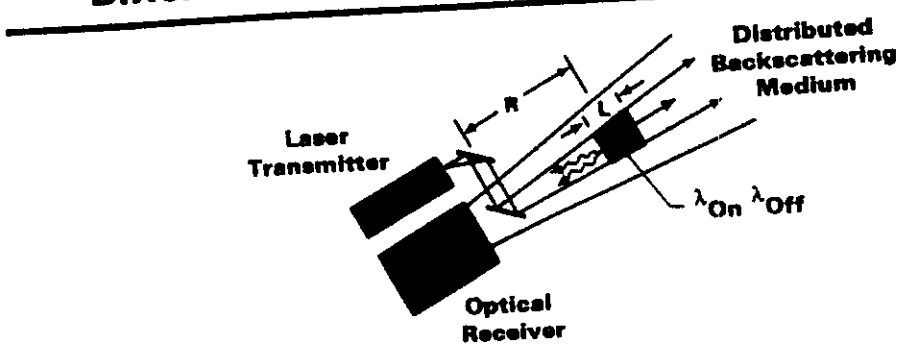

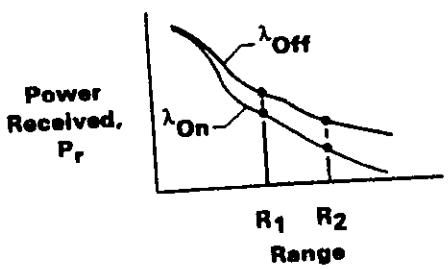

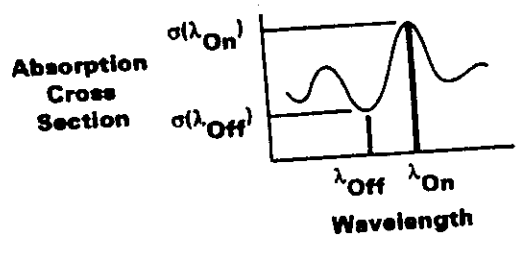

$$N_A = \frac{1}{2(R_2-R_1)\,[\sigma_A(\lambda_{On})-\sigma_A(\lambda_{Off})]} \ln \left[\frac{P_{r_{On}}(R_1) \times P_{r_{Off}}(R_2)}{P_{r_{Off}}(R_1) \times P_{r_{On}}(R_2)} \right]$$

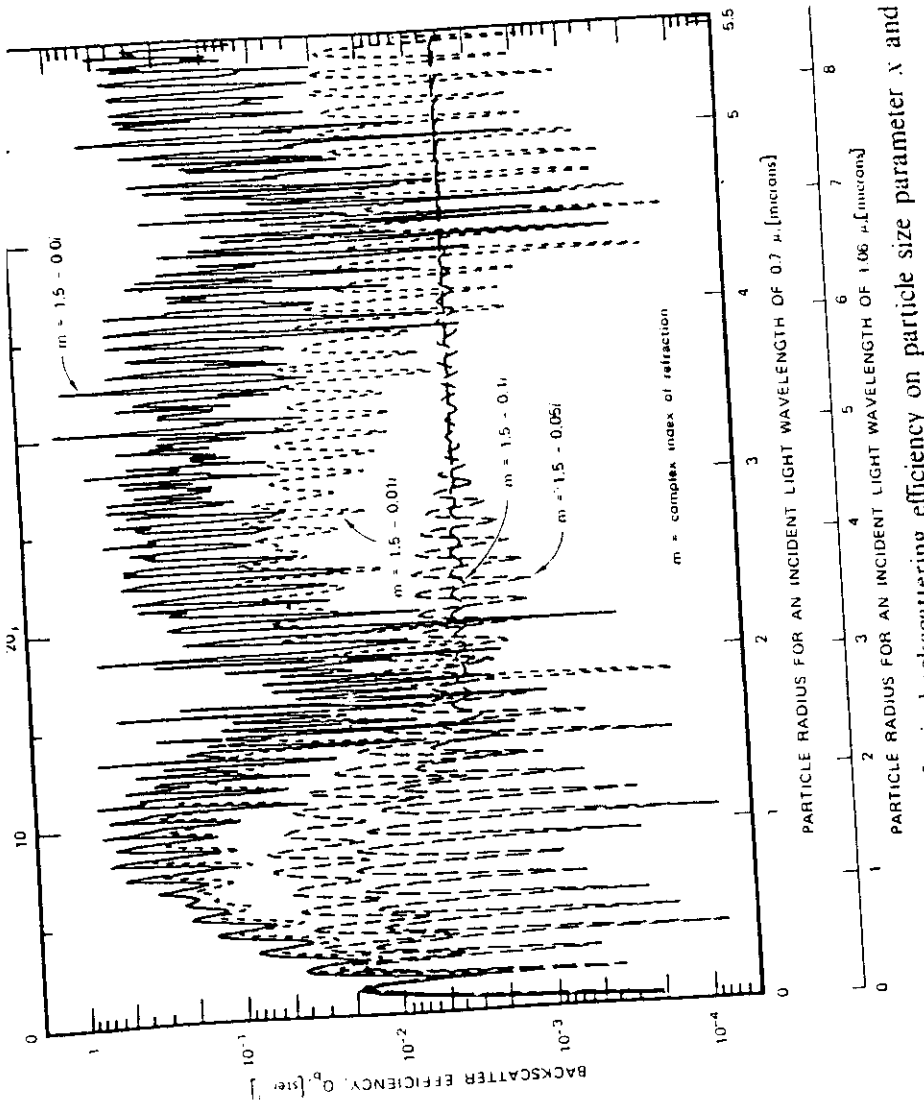

Fig. 4.9. Dependence of mie backscattering efficiency on particle size parameter x and complex refractive index m. ($x = \pi D_p/\lambda$, where D_p is particle diameter)

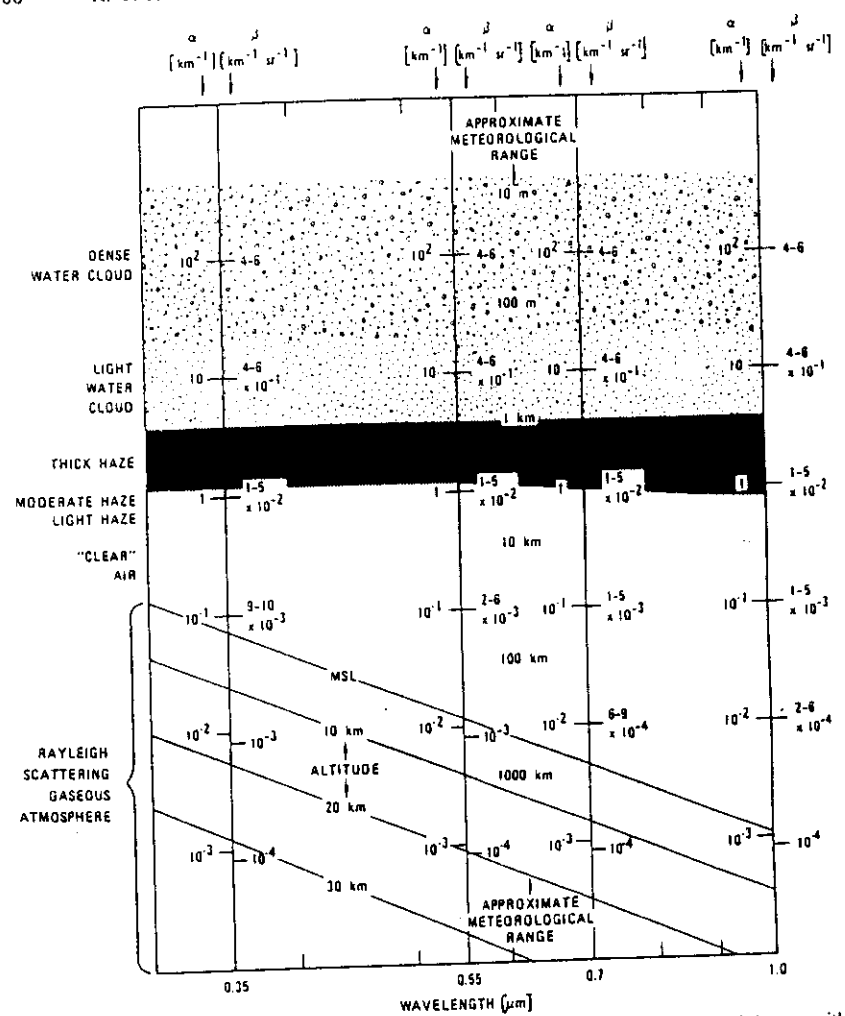

Fig. 4.8. Approximate variation of attenuation and backscattering coefficients with wavelength and atmospheric condition. For haze backscattering coefficients, larger values (for a given attenuation) apply to spherical particles of real refractive particles, partially absorptive particles, or particles with real refractive index $n \approx 1.33$ (e.g., water). [4.26, 33, 39–42, 45–48, 50–54, 67, 68, 107, 113, 115]. For cirrus clouds see [4.125]

and α to atmospheric composition and state is explored in Subsections 4.3.1 and 4.3.2 below. First, however, we present Fig. 4.8, which shows typical values of β and α for a range of wavelengths and atmospheric conditions. These values, along with the parameters of a particular lidar (cf. Table 4.1), may be substituted into the lidar equation (4.1) to obtain performance estimates under various conditions.

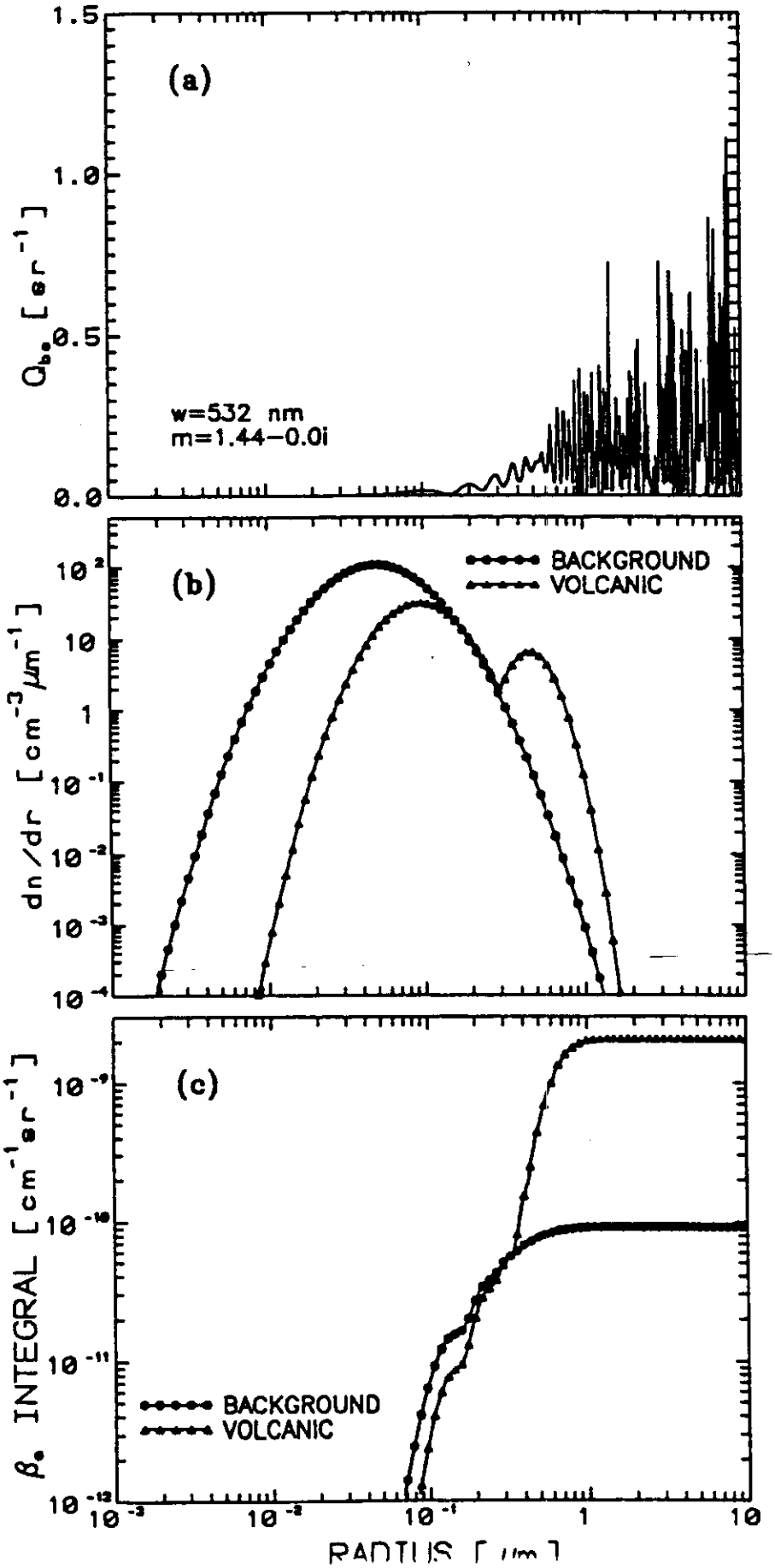
(a)
w=532 nm
m=1.44−0.0i
Q_{bs} [sr^{-1}]
(b)
BACKGROUND
VOLCANIC
dn/dr [cm^{-3}μm^{-1}]
(c)
BACKGROUND
VOLCANIC
β_s INTEGRAL [cm^{-1}sr^{-1}]
RADIUS [μm]

CHARLSON, 1995

THE NATURE OF AEROSOLS AND THEIR EFFECTS

The atmospheric aerosol consists of super-micrometer-(μm) and submicrometer-sized particles of liquid and solid materials suspended in the air. Both natural and anthropogenic materials occur in the aerosol particles; most particles larger than ca. 1 μm are produced mechanically (e.g., windblown soil dust and sea salt from sea-spray and bursting bubbles) and particles smaller than ca. 1 μm are dominantly formed by condensation (e.g., low-temperature condensates, such as sulfate from atmospheric oxidation of SO_2, and high-temperature condensates like soot and smoke from partial combustion). The super- and submicrometer materials are partially mixed by processes in the atmosphere (e.g., coagulation and cloud coalescence) and are removed mainly by cloud and precipitation processes. Climatically relevant particles occur throughout the stratosphere and troposphere in number concentrations that range from tens to tens of thousands of particles per cubic centimeter. While in the atmosphere, the aerosol particles physically affect the heat balance of the Earth, both *directly* by reflecting and absorbing solar radiation and by absorbing and emitting some terrestrial infrared radiation and *indirectly* by influencing the properties and processes of clouds and, possibly, by changing the heterogeneous chemistry of reactive greenhouse gases (e.g., O_3). Substantial perturbation of the sulfate aerosol has occurred due to anthropogenic SO_2. Other aerosol sources also are climatically important, including biomass combustion, volcanoes, and dust storms. It is of particular significance that this meeting emphasized two key aerosol types that cause climate forcing (as defined above), namely anthropogenic and volcanic aerosols. In order to separate their effects from natural variability, it also was necessary to compare them to natural aerosols.

The functional relationships of the aerosol forcings to the source strengths of aerosol particles or their precursor gases are somewhat different for the clean versus the polluted case. The direct effect increases approximately linearly with aerosol number or mass concentration for the typical small optical depths observed in either clean or polluted locations, but (as pointed out by Toon and by King et al., both this volume) the indirect effect goes as the logarithm of the number concentration of particles acting as cloud condensation nuclei (CCN). This is why, although a doubling of industrial SO_2 emissions may produce direct and indirect effects of comparable magnitude in polluted regions of the Northern Hemisphere (NH), by contrast in remote marine regions the indirect effect of doubling dimethylsulfide emissions far exceeds the direct effect.

EVIDENCE FOR AEROSOL EFFECTS

There are many independent lines of evidence supporting the hypothesis that a significant climate forcing exists due to anthropogenic aerosol. Subdivided by direct

A. Direct Forcing

1. Regional-scale optical depth estimates coupled to a regional-scale atmospheric sulfur model for the eastern United States (Ball and Robinson 1982) yielded an annual average loss of solar irradiance of 7.5% due to sulfate aerosol relative to preindustrial times. This corresponds to a measured 2% to 3% per decade loss of solar irradiance over Europe over the past 40 years (Liepert et al. 1994).
2. A calculated global direct cooling of 2–3 K due to "background aerosol" (Coakley et al. 1982) can be combined with current realization that ca. half of the "background" optical depth is due to anthropogenic sulfate and organic aerosols (Andreae 1995) to yield an estimate that a 1–1.5 K global mean cooling exists due to anthropogenic aerosol.
3. AVHRR satellite imagery over the oceans shows an enhanced aerosol optical depth in the NH versus Southern Hemisphere (SH), with maxima in the vicinity of industrial regions and downwind of the Sahara Desert (Durkee et al. 1991; Stowe and Husar, pers. comm.). See Plate 1.1. Simultaneously, the Stratospheric Aerosol and Gas Experiment (SAGE) shows ca. a factor of three summertime enhancement of aerosol extinction in the NH mid-latitude upper troposphere (Kent et al. 1991).
4. In recent decades, the SH surface temperature appears to have risen more than in the NH (Wigley 1989), contrary to many model predictions for greenhouse gases alone (e.g., Manabe et al. 1980). Relative cooling in industrial regions and the NH mid-latitudes is observed (Engardt and Rodhe 1993; Hunter et al. 1993; Karl et al., this volume) and calculated (Roeckner et al., this volume). Some amount of the decrease in diurnal temperature range over industrial regions also may be explained by aerosol forcing (Karl et al., this volume).
5. Observations show that the stratospheric aerosol from the 1991 eruption of Mt. Pinatubo produced a peak global mean optical depth at 550 nm wavelength of 0.1 to 0.2, which resulted in a measured peak global forcing of ca. -4.5 W m^{-2} in 1992 and a temporary, calculated, *and* observed cooling of the surface of ca. 0.5°C (Lacis and Mishchenko, this volume). Comparable and even larger optical depths (0.1–0.5) are found in industrial regions and are largely attributed to anthropogenic aerosol (Ball and Robinson 1982). SAGE satellite data mapped the global distribution of optical extinction due to stratospheric aerosol from Pinatubo (see Plate 1.2), demonstrating its near-global extent.
6. Studies of visibility indicate increasing extinction from the 1940s to the 1970s due to anthropogenic aerosols in the eastern U.S. (Husar et al. 1981). Typical visually estimated extinction coefficients of $1 - 3 \times 10^{-4}$ m^{-1} along with an estimated scale height of 2 km yield aerosol optical depths of 0.2–0.6 in agreement with observations.
7. Measured light scattering by atmospheric aerosols often is highly correlated with the measured masses of sulfate and organic compounds in the aerosol. A multiple regression analysis for the U.S. yielded a squared correlation

CHARLSON, 1995

coefficient of 0.95 (White 1990). Maps of SO_2 emission, SO_4^{2-} measured aerosol concentration, acidic deposition, and extinction coefficient show geographical coherence over the eastern U.S. (Husar et al. 1981; Charlson et al. 1992a).

8. A coupled mass-balance/radiation, single-box model for anthropogenic sulfate aerosol (Charlson et al. 1990; Charlson et al. 1992) yielded a global mean value of ca. -1 W m^{-2} for the direct forcing with no stated uncertainty.
   Coupled three-dimensional atmospheric chemical/radiation models for anthropogenic sulfate aerosol (Charlson et al. 1991; Pham et al. 1994; Kiehl and Rodhe, this volume) suggest global mean values from ca. -0.3 to -1.2 W m^{-2}, with local values to -10 W m^{-2} over industrial regions. Uncertainty is estimated crudely as up or down by a factor of two. Direct forcing by aerosols from biomass combustion as estimated by a simple box model has an even larger uncertainty but is in a possible range form -0.05 to -0.6 W m^{-2} (IPCC 1994).

B. Indirect Forcing

1. Anthropogenic pollution enhances the CCN population (Hobbs et al. 1974; Radke and Hobbs 1976) and cloud albedo is calculated to be increased due to increased CCN population (Twomey 1971).
2. Continental (polluted?) clouds have higher droplet populations than those in marine air (Pruppacher and Klett 1978) and thus presumably higher albedo for a given liquid water path per item 1 above.
3. Satellite imagery illustrates the enhancement of stratus cloud albedo due to particles emitted by ships (Coakley et al 1987; Radke et al. 1989) as well as due to the plume emanating from an urban region into a marine stratus cloud deck (Durkee 1989).
4. Marine low clouds in the NH have smaller (and thus, theoretically, larger numbers of) droplets and higher albedo than those in the SH (Han et al. 1994). The suggested ratio of droplet populations in the NH to that in the SH is 1.1 to 1.5.
5. A sensitivity test of a model in which the CCN concentration is estimated to be a function of sulfate aerosol mass concentration suggests a NH mean forcing of ca. -1.3 to -2.5 W m^{-2} due to the known amounts of anthropogenic sulfate aerosol. The uncertainty was stated to be large (Boucher and Rodhe 1994). A comparison of sulfate aerosol to CO_2 forcing suggests a cooling that is comparable in magnitude (Kaufman et al. 1991). Again, large uncertainties are suggested.

Numerous papers appeared in the 1970s and 1980s addressing parts of the aerosol/climate problem and presaging the developments of the period 1990–1994. One in particular is noteworthy because it was first presented at a Dahlem workshop. Grassl (1988) presented zonal-mean climate forcing calculations, including estimates of direct and indirect effects, concluding that significant anthropogenic forcing exists in

These lines of evidence taken together, along with a lack of counter evidence, provide a basis for concluding that a significant direct forcing does exist due to anthropogenic aerosol but has a large uncertainty. The Intergovernmental Panel on Climate Change (IPCC) suggests that the global mean direct forcing due to anthropogenic sulfate and biomass combustion aerosol may lie in the range -0.3 to -1.5 W m^{-2} (IPCC 1994). While this is opposite in sign and of important magnitude compared to the current positive forcing by anthropogenic greenhouse gases (2.3 ± 0.35 W m^{-2}), we caution that the global mean aerosol forcing cannot be simply subtracted from greenhouse gas forcing due to their large geographical, seasonal, and diurnal variability (see Ramaswamy et al., this volume). By comparison, negative indirect forcing is likely to be present, may be of important magnitude, but is too uncertain to quantify (IPCC 1994). In both cases—direct and indirect—the uncertainties are unacceptably large and present serious limitations to the modeling of climate.

POLICY IMPLICATIONS

The total indicated loss of solar energy due to the direct and indirect effects of sulfate and biomass combustion aerosols alone clearly could be comparable in magnitude but is opposite in sign to the trapping of energy by infrared-light-absorbing, anthropogenic CO_2. The changes in global energy balance due to other tropospheric aerosol components, such as light-absorbing (soot) carbon and anthropogenic soil dust, may be important but are less well studied. Thus, climate forcing by anthropogenic aerosols poses both large uncertainties in climate forecasting and puzzling difficulties in managing emissions of both aerosols and greenhouse gases.

This hypothetical diminution of the globally averaged warming confounds the problem of setting world policy on greenhouse gas and other pollutant emissions. Negative forcing by anthropogenic SO_4^{-2} aerosol also implies that control of SO_2 emissions (e.g., to diminish acid rain) may cause increased warming (Wigley 1989). Ironically, the short (few-day) lifetime of aerosol particles in the troposphere, compared to the long time for equilibrating CO_2 with the ocean (decades to a century) also implies that measures to limit fossil-fuel combustion may cause enhanced warming (IPCC 1992). Even if the world achieved constancy in fossil-fuel combustion (and hence in CO_2 and SO_2 emissions), CO_2 and its warming effect would continue to rise until the ocean surface equilibrates with the atmosphere CO_2, while constant SO_2 emission would result in almost immediate constancy in SO_4^{-2} and its attendant cooling effects. An action taken to decrease "global warming" may appear to cause increases instead, but only for a few decades. Thus, understanding and quantifying the aerosol forcing of climate are essential components in national and international planning to avoid deleterious or calamitous effects of human-caused climate change. One of the additional goals of this workshop thus was to aid in defining the research questions that are most central to policy decisions.

d'ALMEIDA, 1991

CHARACTERIZATION

TABLE 2.1 Source strength of atmospheric aerosol particles in Tg/yr for radii smaller than 100 μm

Aerosol component	Source strength	Reference
Natural aerosol sources		
o Extraterrestrial dust	10	SCEP (1970)
	16 – 18	Cameron (1981)
o Sea – salt	1000	SMIC (1971), Junge (1979)
	10000	Blanchard and Woodcock (1980)
o Desert dust	500	Peterson and Junge (1971)
	1800 – 2000	d'Almeida (1986)
o Volcanic debris	25 – 150	SMIC (1971)
	250	SCEP (1970)
o Biogenic/biologic	80	Bach (1976)
o Gas to Particle Conversion (sulfate, organics, nitrate)	570	SCEP (1970)
	345 – 1100	SMIC (1971)
Subtotal	3266 – 13448	
Man – made aerosol sources		
o Direct particulate emission	10 – 90	SMIC (1971)
	275	SCEP (1970)
o Gas to Particle Conversion (carbonaceous substances, organics, sulfate, nitrate)	175 – 325	SMIC (1971)
o Forest fires and slash – burning debris [1)]	3 – 150	SMIC (1971)
Subtotal	188 – 565	
Total	3454 – 14013	

1) includes unknown amount of indirect natural contributions

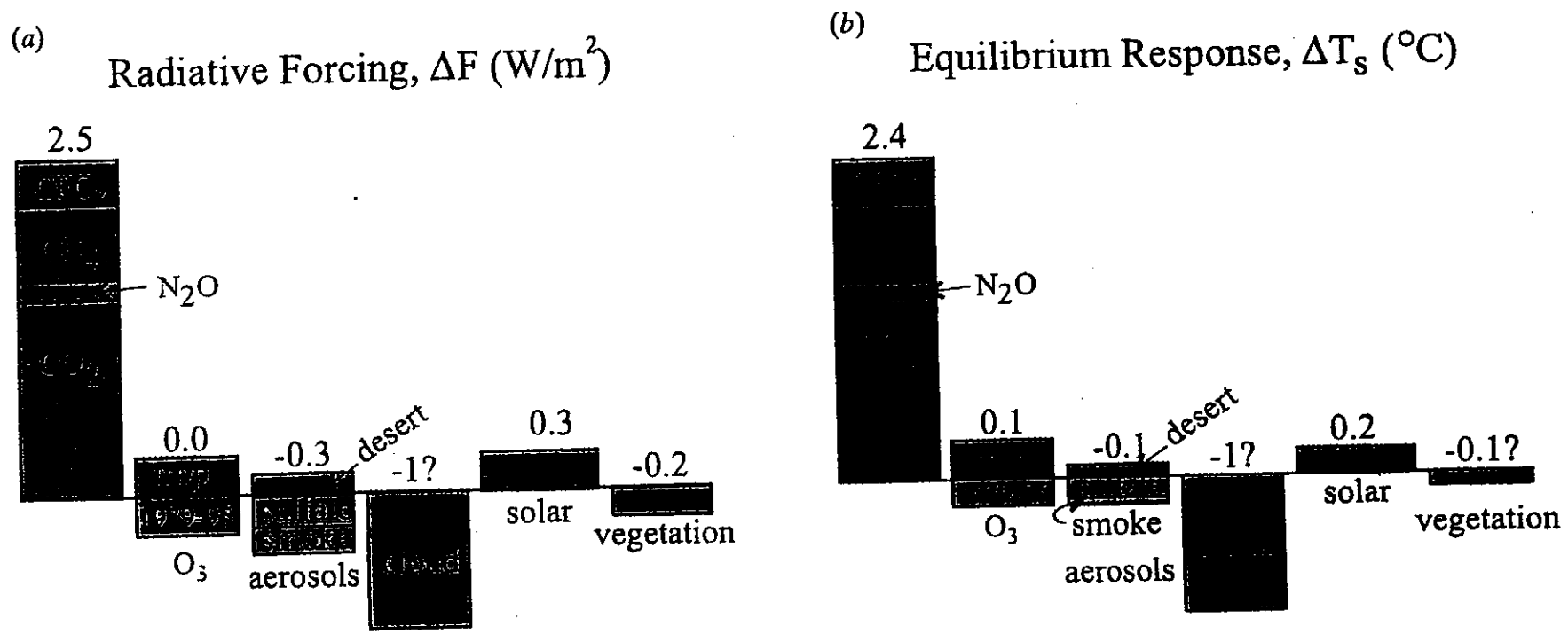

Figure 6. Radiative forcings (*a*) and equilibrium surface air temperature changes (*b*) calculated for atmospheric changes occurring between the pre-industrial era and 1995, the temperature changes being based on a GCM with sensitivity 3.8 °C for doubled CO_2. Greenhouse gas changes are CO_2 (280 to 359 ppm), CH_4 (700 to 1730 ppb), N_2O (275 to 312 ppb), CFC-11 (0 to 262 ppt), CFC-12 (0 to 518 ppt), other CFCs after Hansen *et al.* (1997). Ozone pre-industrial to 1980 change based on Crutzen (1994).

CHARLSON (Ed.), 1995

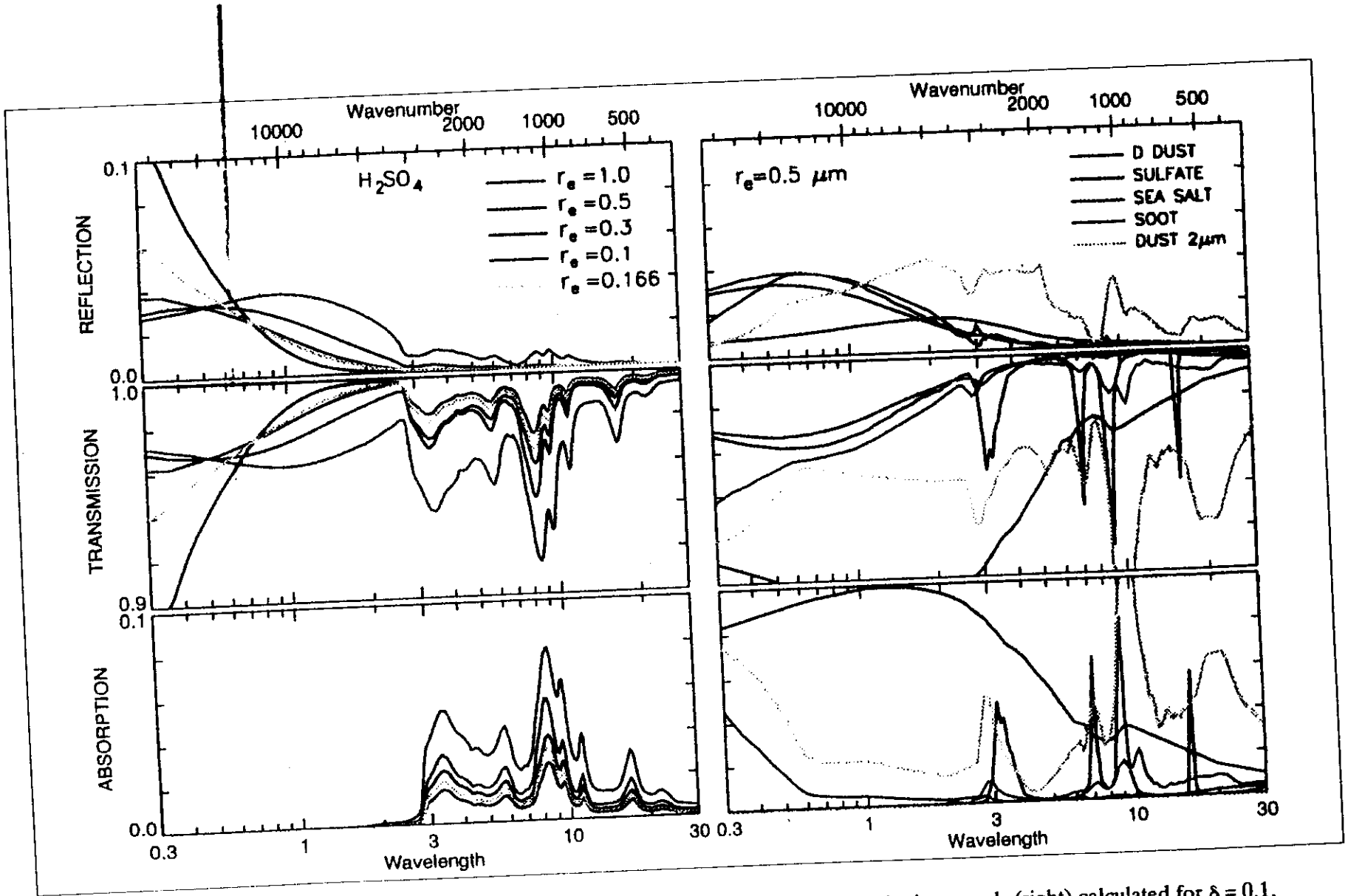

Plate 2.5 Globally integrated radiative properties for H_2SO_4 (left) and representative tropospheric aerosols (right) calculated for $\delta = 0.1$.

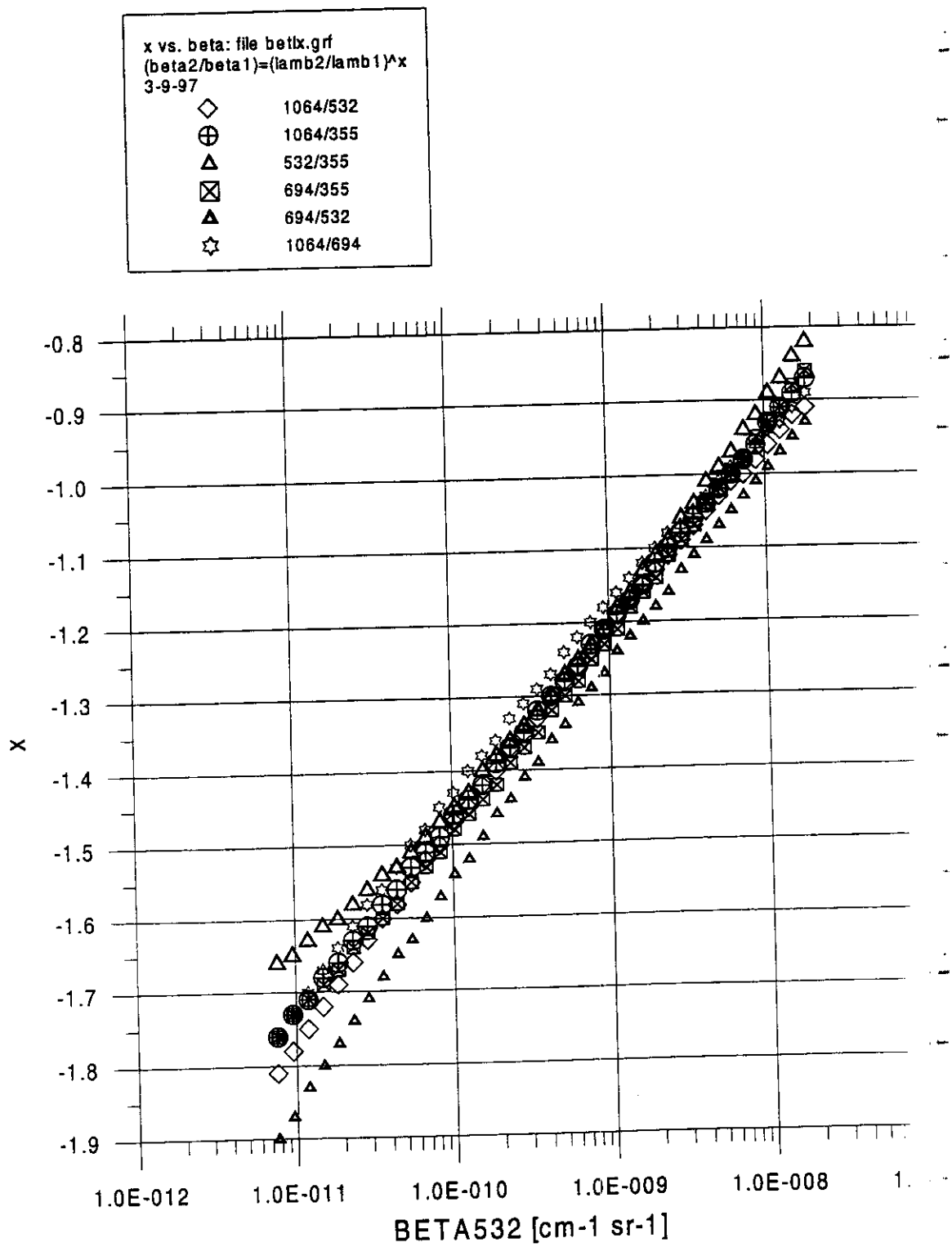
x vs. beta: file betlx.grf
(beta2/beta1)=(lamb2/lamb1)^x
3-9-97
1064/532
1064/355
532/355
694/355
694/532
1064/694
-0.8
-0.9
-1.0
-1.1
-1.2
-1.3
-1.4
-1.5
-1.6
-1.7
-1.8
-1.9
x
1.0E-012
1.0E-011
1.0E-010
1.0E-009
1.0E-008
BETA532 [cm-1 sr-1]

GOBBI ET AL. JGR 199[illegible]

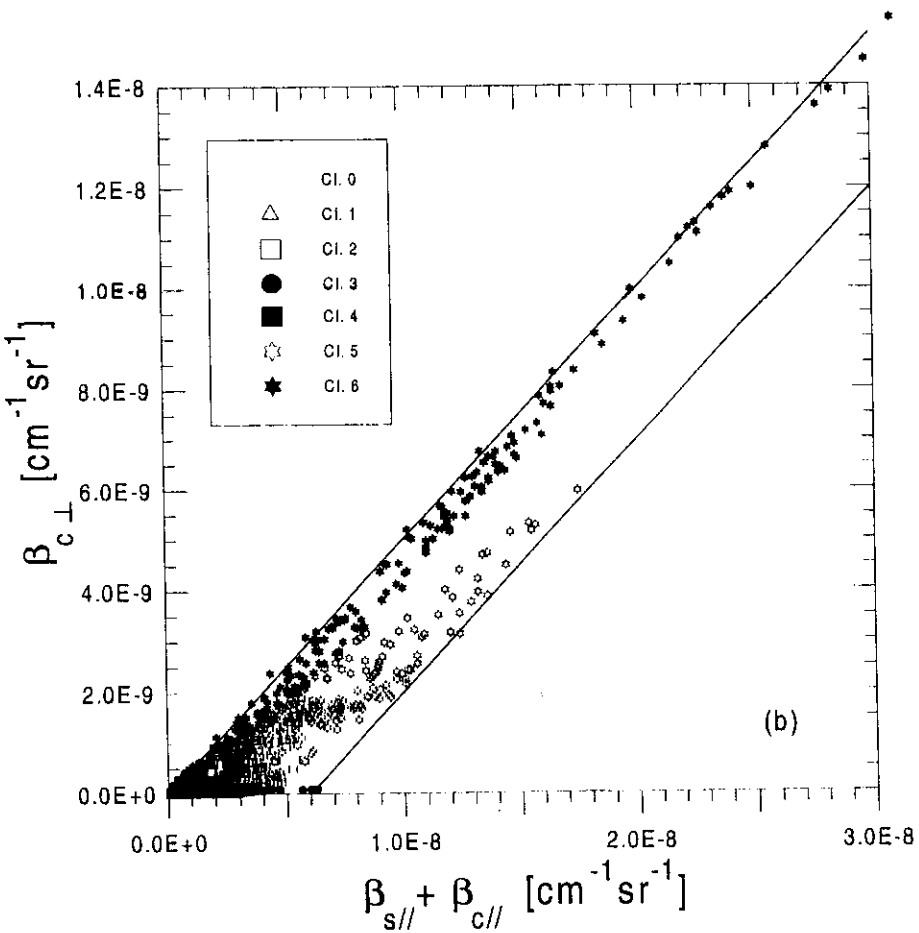

FIG. 2b

fig2b (95y9bcbs.grf)
22-7-97 allbit.dat

```
########## User: [redacted]
##### Title: 560-1
#####  Date: Tue 12:09 Oct 19, 1999
#####   Job: tekcolor-560
#####
```

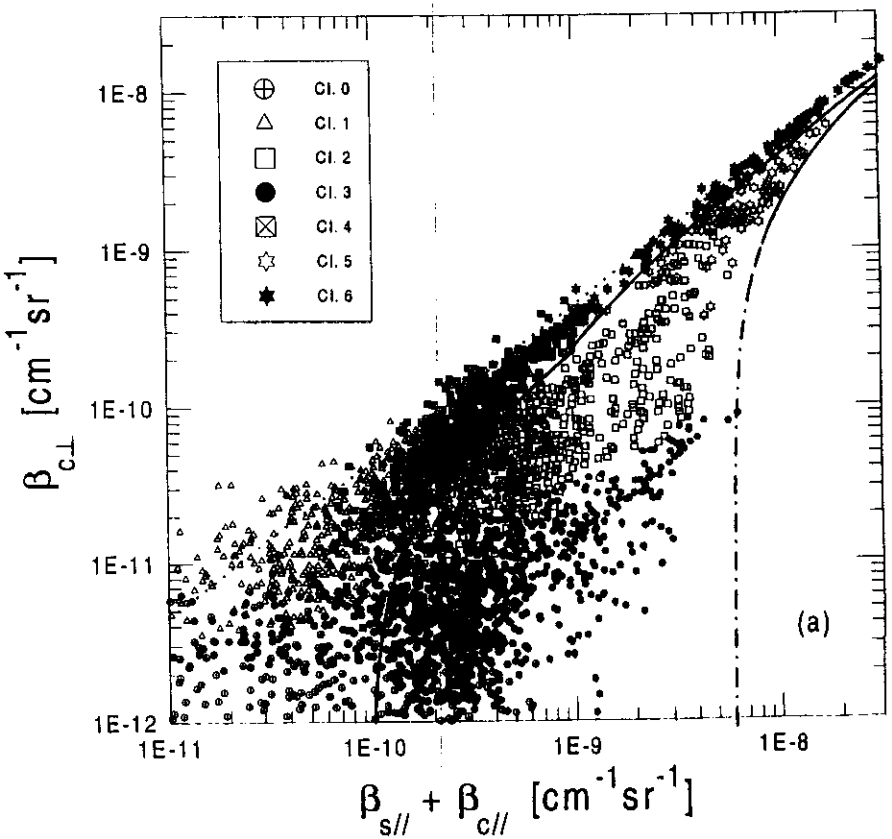

FIG. 2a

fig2a.grf
14-1-98 allbit.dat

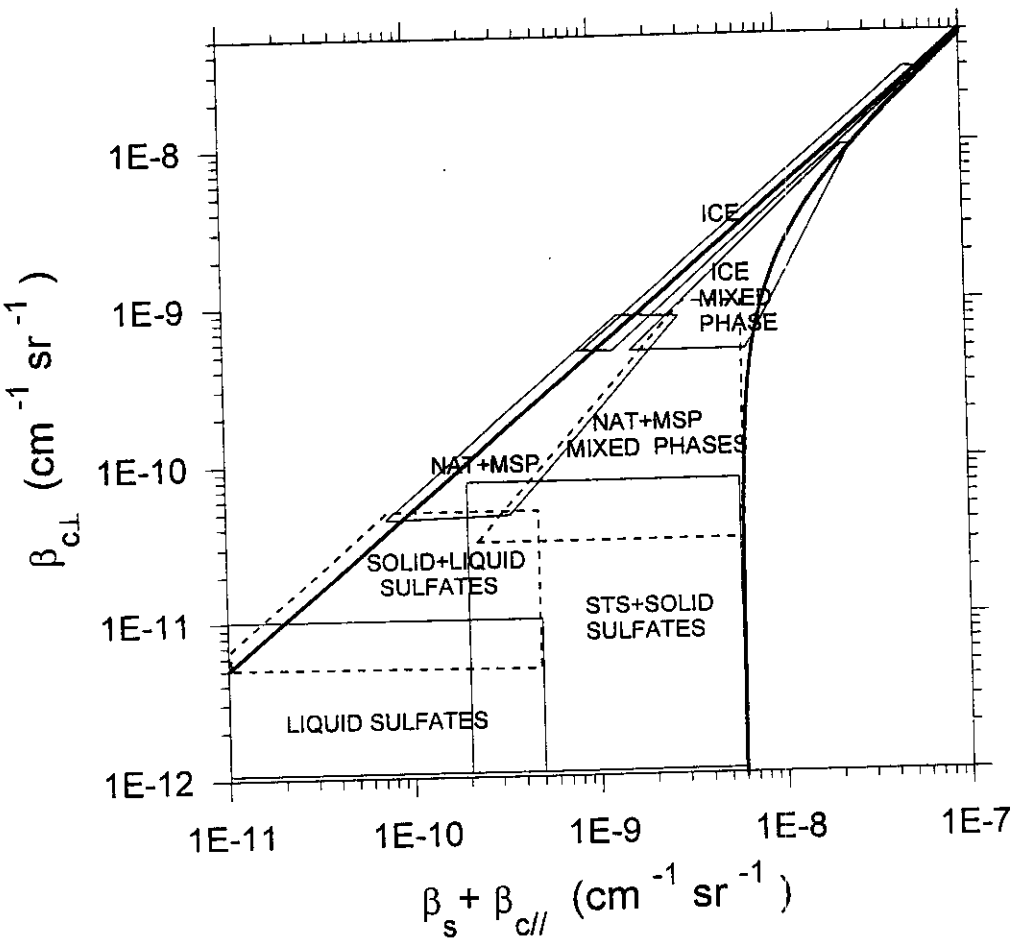

METHOD OF PERPENDICULAR CROSS SECTION COORDINATES APPLIED TO THE STUDY OF POLAR STRATOSPHERIC CLOUDS

(Gobbi, Applied Optics, 37, 5505, 1998)

Lognormal size-distribution:

$$\frac{dN_i(r)}{d\log r} = \frac{N_i}{\sqrt{2\pi}\log\sigma_i}\exp\left(-\frac{(\log r - \log r_{Mi})^2}{2(\log\sigma_i)^2}\right)$$

*MARITIME**	*Size-distribution*				*Refractive index*	
component	mode	parameter				
		$r_{Mi}(\mu m)$	σ_i	$N_i/N_{tot}(\%)$	$N_{tot}(cm^{-3})$	$m_{\Re e}$	$m_{\Im m}$
Sea-salt	1	0.05 - 0.1	1.4 - 2.03	5 - 70	500-800	1.5	$6.9\cdot10^{-9}$
	2	0.4 - 0.6	1.4 - 2.03	0.4 - 3.0			
sulfates	3	0.02 - 0.1	1.4 - 2.03	30 - 90		1.43	$1\cdot10^{-8}$

DUST	*Size-distribution*				*Refractive index*	
component	mode	parameter				
		$r_{Mi}(\mu m)$	σ_i	$N_i/N_{tot}(\%)$	$N_{tot}(cm^{-3})$	$m_{\Re e}$	$m_{\Im m}\cdot10^{-3}$
desert-dust	1	0.02-0.08	1.5 - 2.1	93 -98	200-1500	1.5 - 1.55	4 -8
	2	0.2 - 1.5	1.5 - 2.0	2 - 7			

$$r_{\text{eff}} = \frac{1}{G} \int_{r_{\min}} dr r \pi r^2 n(r) \tag{12}$$

and the effective variance defined as

$$v_{\text{eff}} = \frac{1}{G r_{\text{eff}}^2} \int_{r_{\min}}^{r_{\max}} dr \left(r - r_{\text{eff}}\right)^2 \pi r^2 n(r), \tag{13}$$

where G is the average cross-sectional area:

$$G = \int_{r_{\min}}^{r_{\max}} dr \pi r^2 n(r). \tag{14}$$

This means that different size distributions having the same values of r_{eff} and v_{eff} have similar single-scattering properties. In view of many different analytical parameterizations of natural size distributions suggested in

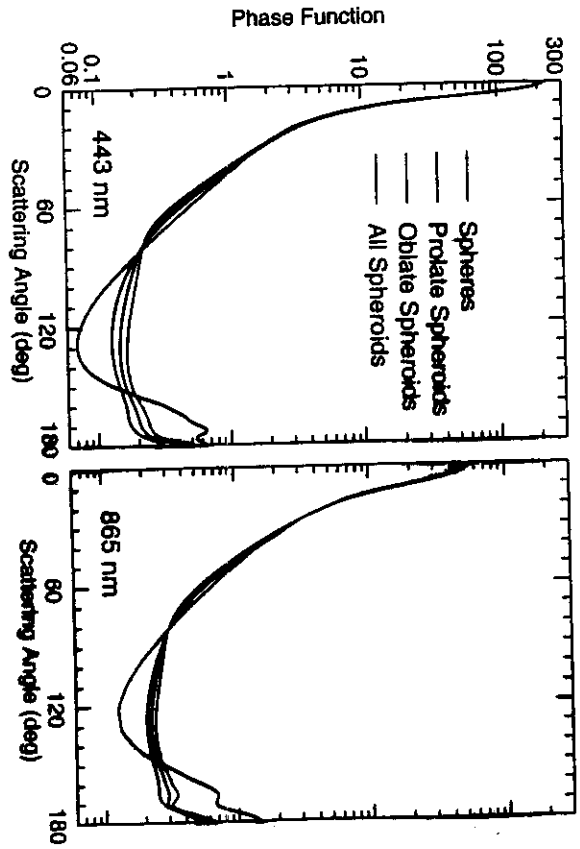

Plate 3. The upper panels demonstrate the effect of varying width of the spheroid aspect-ratio distribution and show ensemble-averaged phase functions for equiprobable shape mixtures of prolate and oblate spheroids with different aspect-ratio ranges. For all shape distributions the aspect-ratio step size is equal to 0.1. The lower panels show phase functions for polydisperse spheres and ensemble-averaged phase functions for equiprobable shape mixtures of prolate spheroids (green curve), oblate spheroids (blue curve), and prolate and oblate spheroids (red curve) with aspect ratios ranging from 1.2 to 2.4 in steps of 0.1. All curves were computed for the modified lognormal distribution of surface-equivalent-sphere radii

Mishchenko et al. JQSRT, Vol. 55, No. 5, pp.

MISHCHENKO ET AL., 1997

RING BY NONSPHERICAL AEROSOLS

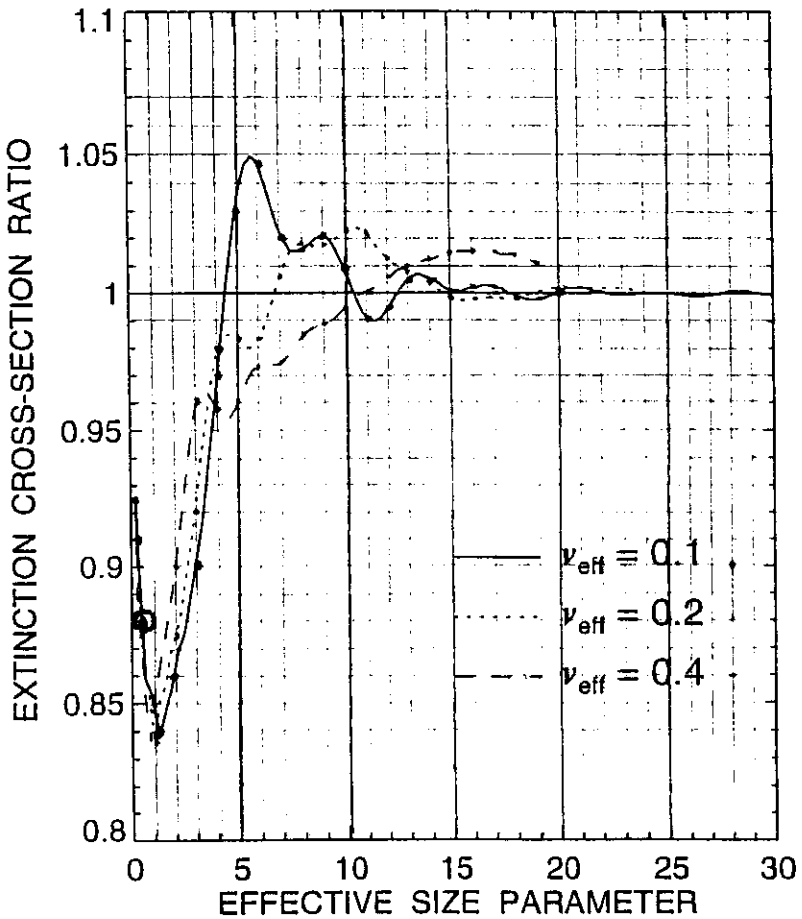

Figure 4. The ratio of the extinction cross section for a shape mixture of polydisperse, randomly oriented nonspherical aerosols relative to that for surface-equivalent spheres versus effective size parameter. The curves are computed assuming the power law size distribution with effective variance ν_{eff} equal to 0.1, 0.2, and 0.4 and the equiprobable mixture of prolate and oblate spheroids with

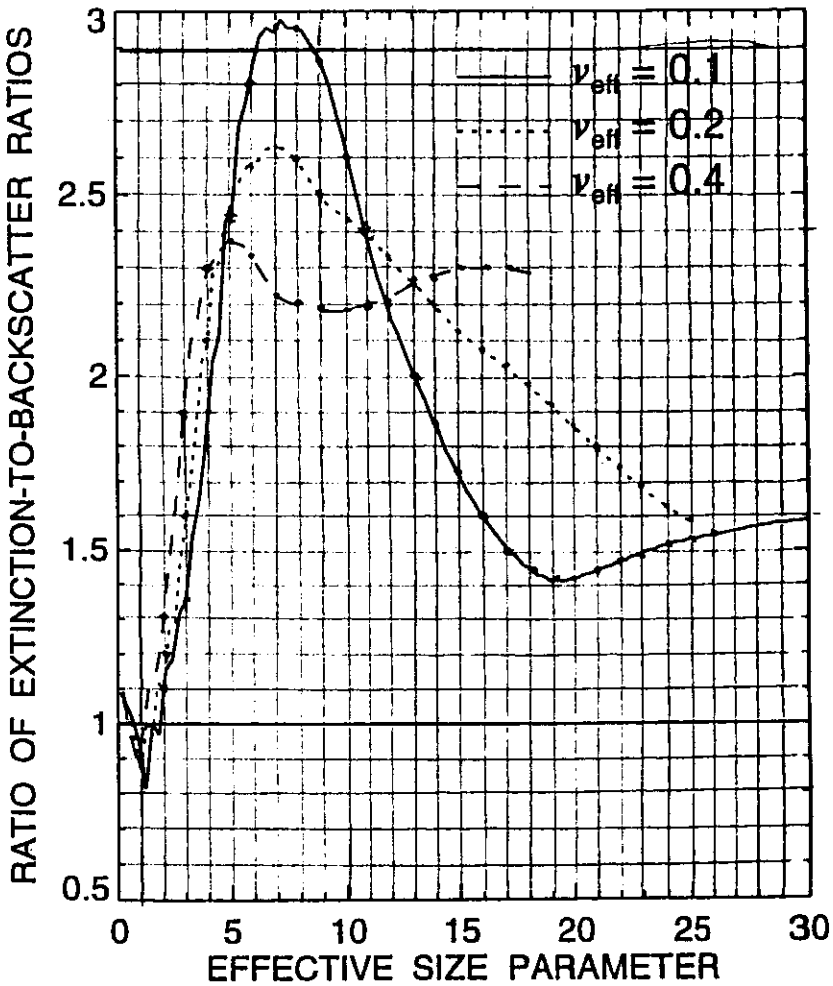

Figure 10. As in Figure 4, except for the ratio of the nonspherical to the spherical extinction-to-backscatter ratios.

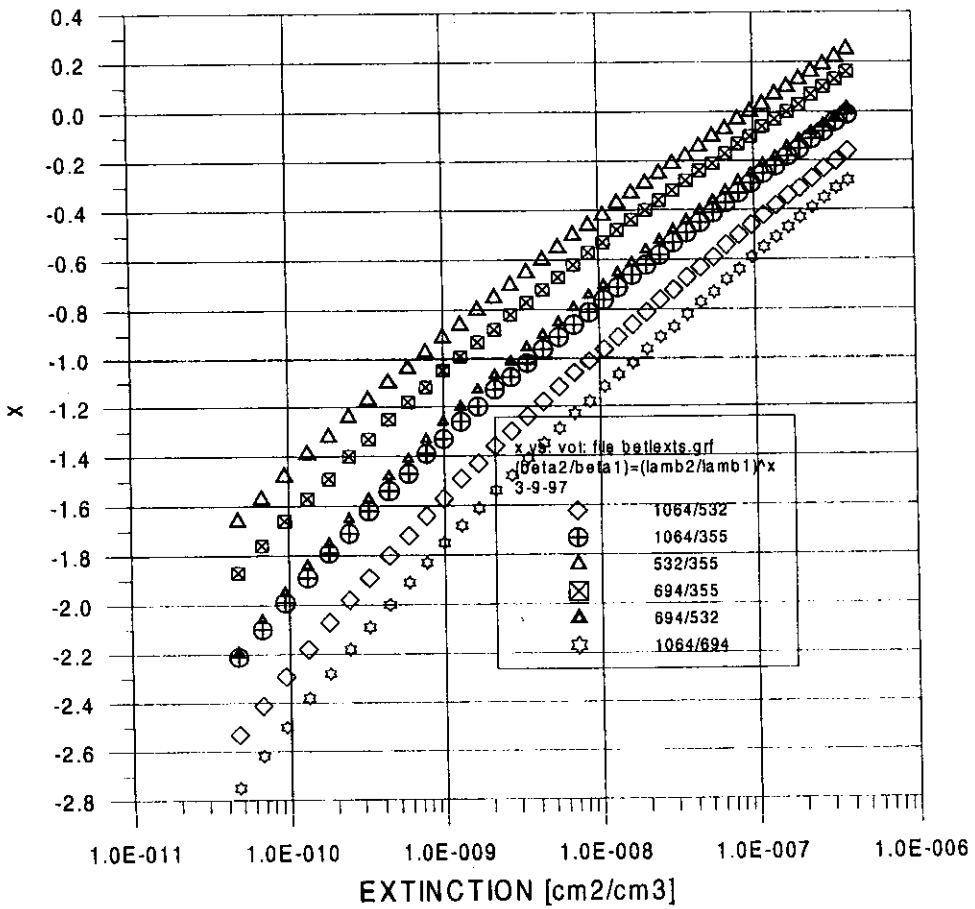

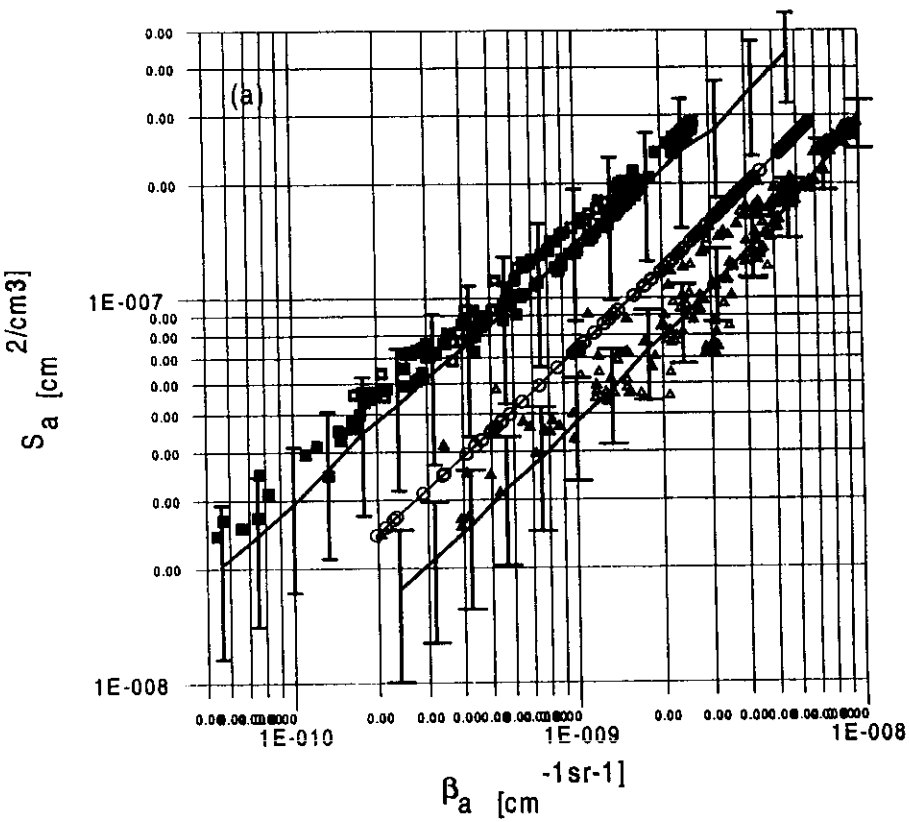

Fig. 5a

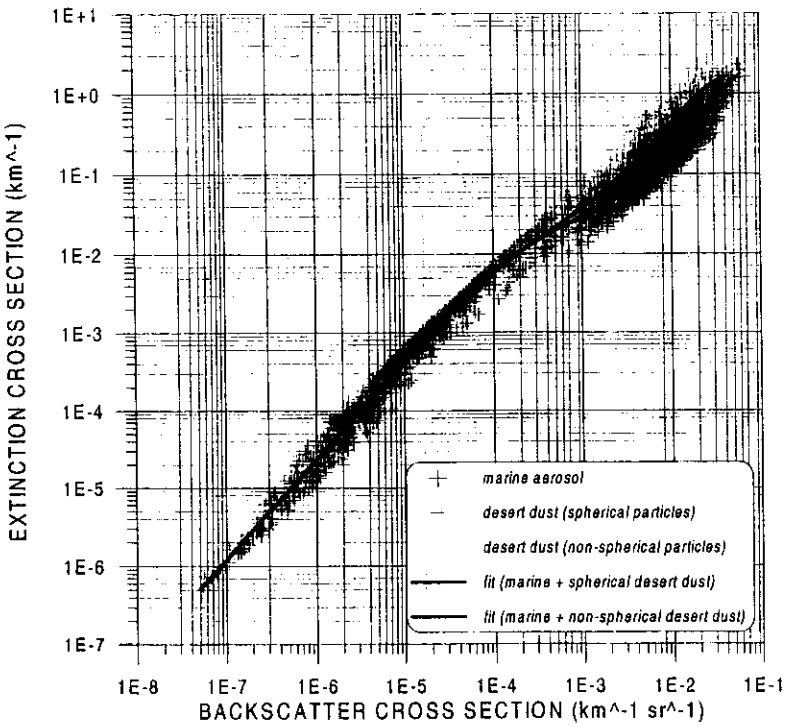

Extinction model output results for marine and desert-dust aerosols (plotted as function of backscattering) and fitted curves. Each curve has been obtained fitting 20.000 (marine) + 20.000 (desert-dust) points (1/20 plotted above).

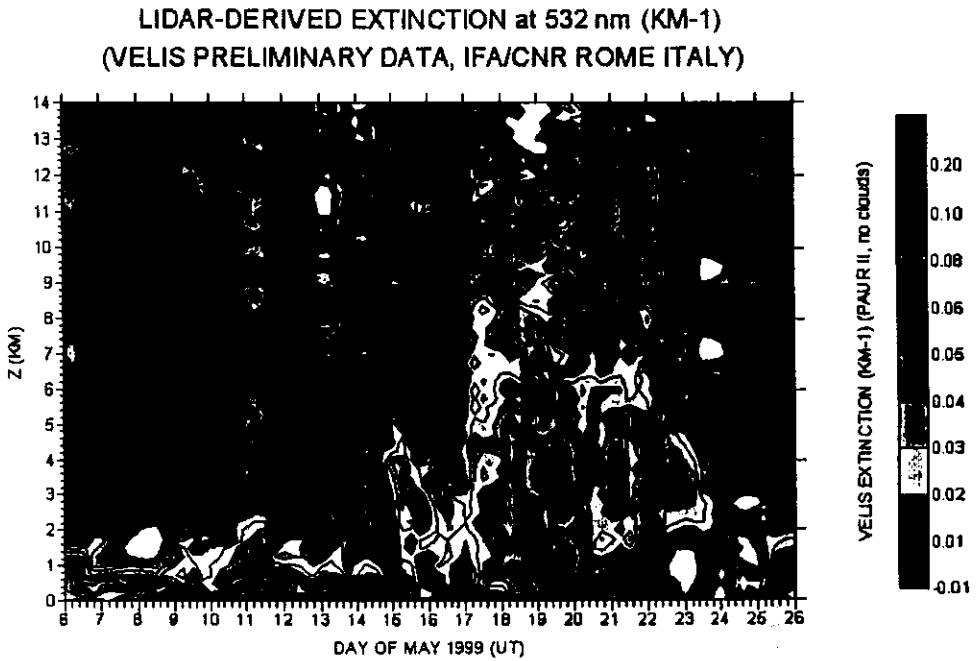

Desert dust event observed by the VEhicle-mounted Lidar System (VELIS), during the PAU'R II campaign at Crete (36N-23E) in May 1999. Only cloudless profiles are considered.
VELIS is a miniaturized polarization lidar designed for the observation of atmospheric aerosols in the range 200 m - 25 km.
Extinction values are derived from lidar backscatter by means of a model providing functional relationships between extinction and backscatter for marine and desert dust aerosols. The model follows the approach adopted in Gobbi, Appl. Opt., 37, 4712, 1998.
This data is to appear in Gobbi et al., Atmos. Env., 2000.

AEROSOL INDEX FROM TOMS DATA

$$AI = -100\left[\log_{10}\left(\frac{I_{340}}{I_{380}}\right)_{meas} - \log_{10}\left(\frac{I_{340}}{I_{380}}\right)_{calc}\right]$$

Earth Probe TOMS
Absorbing Aerosol Index for May 10, 1999

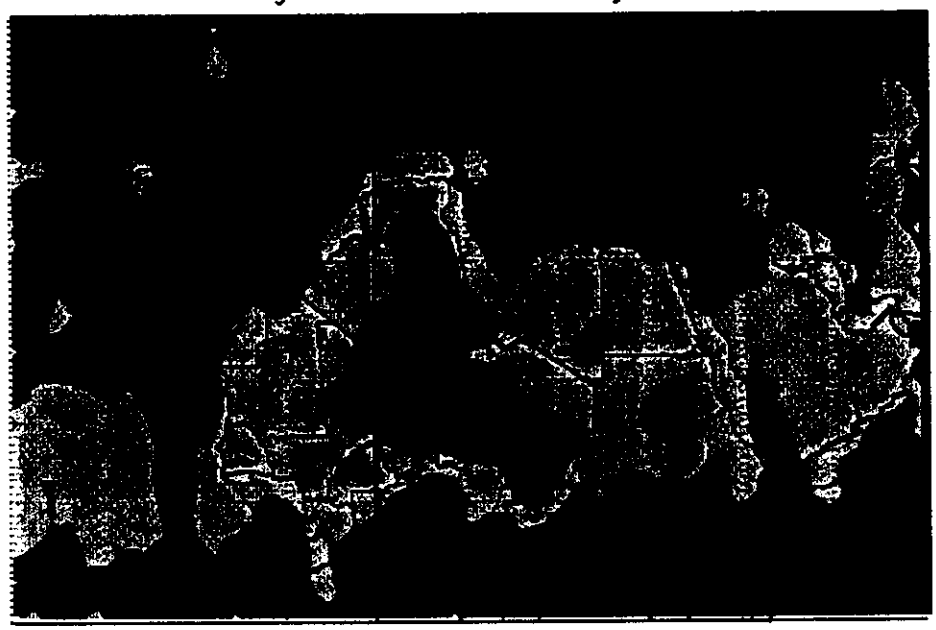

0.7 1.1 1.5 1.9 2.3 2.7 3.1>
Aerosol Index

Goddard Space Flight Center

Earth Probe TOMS
Absorbing Aerosol Index for May 20, 1999

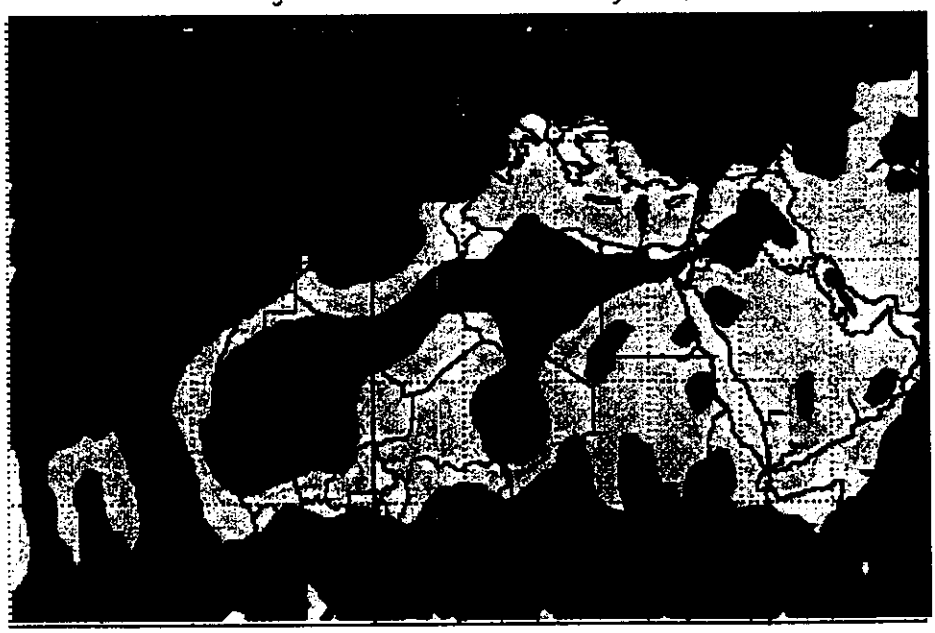

0.7 1.1 1.5 1.9 2.3 2.7 3.1>
Aerosol Index

Goddard Space Flight Center

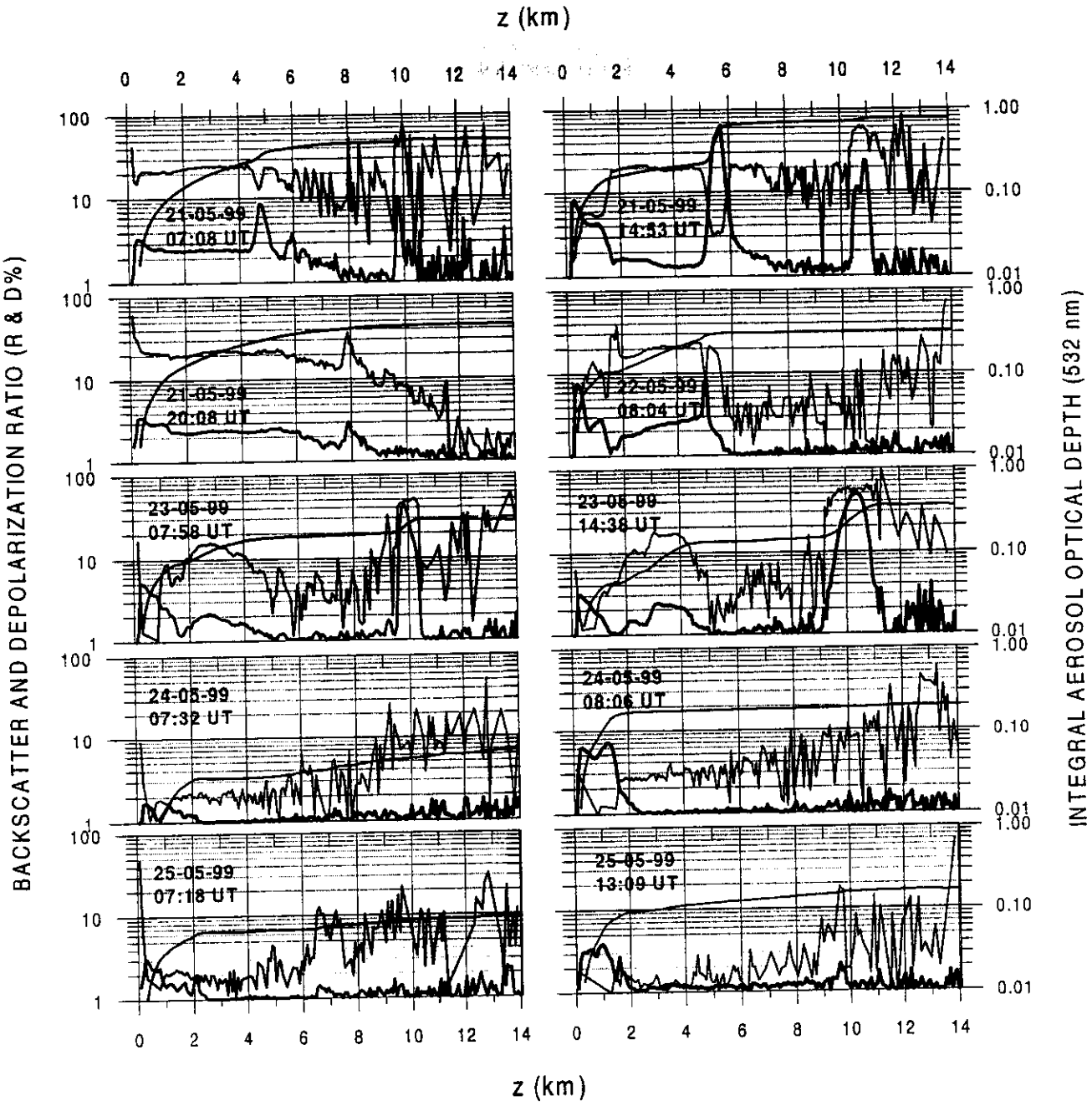

Figure 2: Verical profiles obtained by Velis during the PAUR II campaign. Black line: lidar backscatter ratio (R); blue line: lidar depolarization ratio (D); red line: aerosol optical depth (from the ground to z).

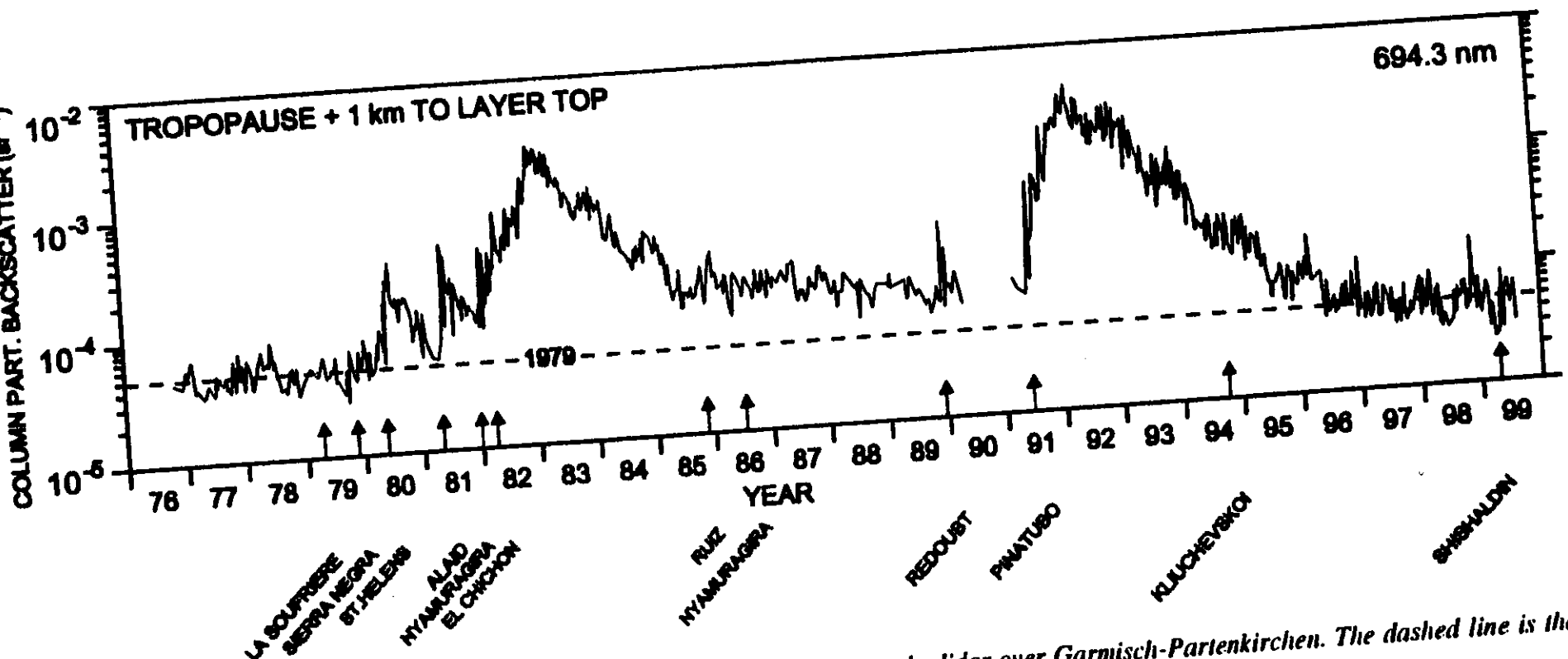

Figure 2. Integrated particle backscatter of the stratospheric aerosol layer, seen by lidar over Garmisch-Partenkirchen. The dashed line is the 1979 mean. Volcanic eruptions are marked. Annual cycles are caused by the annual tropopause variation.

Lidar Sensors

Program Carrier	Circa	Channels	Laser(s) (*tunable)	Measurement of Species
GND. based, 48 inch	1970	2	Ruby @ 347 & 694 nm	Aerosols/ N_2
Aircraft Electra 990	1978	3	Ruby, YAG, YAG/ Dye @ 1064, 720*, 694, 600*, 532, 347, 300* nm	Aerosols H_2O/O_3
LASE, ER 2	1994	3	Ti: Al_2O_3 @ 815 nm	H_2O/Aerosols
LITE, Shuttle	1994	3	YAG @ 1064, 532, 355 nm	Aerosols/clouds Density
ESSP	TBD	3	YAG @ 1064, 532,	Aerosols/clouds

LITE Directory
Home Page
Mission Overview
Data User's Guide
Data FAQ's
Science Steering Group
Instrument
Publications
Images
Photos
Photos and Images
Data Gallery
Meta Data
ISDB Data
Site Map

LITE Instrument

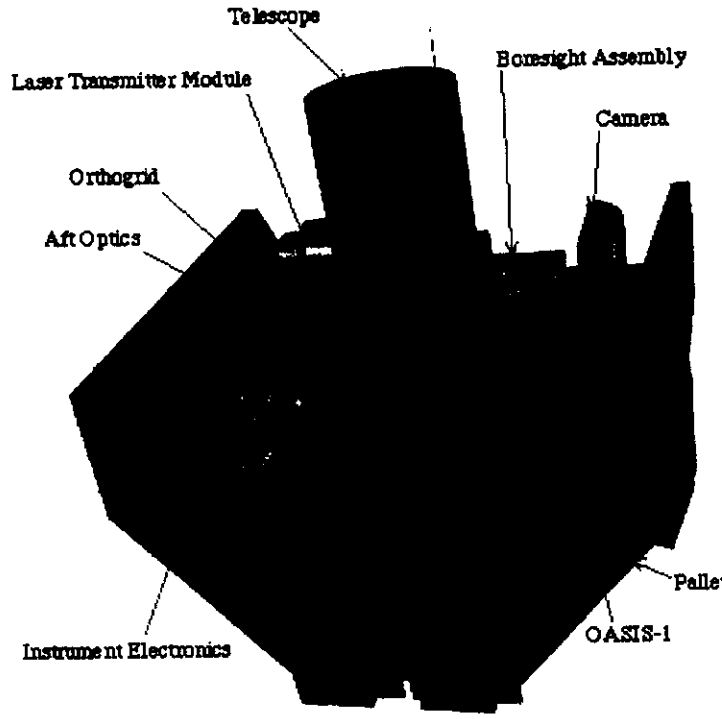

The LITE instrument was carried in the Shuttle cargo bay on a standard Spacelab pallet. T instrument was mounted on an orthogrid platform attached to the pallet by 52 struts. The orthogrid is a support platform for the instrument subsystems and was designed to be imr to thermal deformations which could affect optical alignment. A description of the major subsystems follows.

Receiver Assembly

The receiver includes a one meter telescope and an aft-optics package. The telescope col laser light scattered from the atmosphere, and brings it to focus in the aft optics. The aft includes wavelength selective optics to separate the return signal into its three color components. The 532 nm and 355 nm detectors are photomultiplier tubes, while the 106 detector is a silicon avalanche photodiode.

Boresight Assembly

The boresight assembly consists of a two-axis motor-driven prism. Its purpose is to align laser beam to the telescope field-of-view so that both point to the same column of atmos

Laser Transmitter Module (LTM)

The LTM consists of two flash lamp-pumped, Q-switched Neodymium:YAG lasers wh simultaneously at the three harmonically related wavelengths of 1064 nm (infrared), 53 (visible green), and 355 nm (ultraviolet). The two-laser system provides redundancy in one laser fails. Only one laser operates at a time.

Orbiter Experiments Autonomous Support

REFERENCES:

A list of over 800 lidar-related papers can be found at the www site:
http://www.osa.org/HOMES/GENERAL/BIBLIO/lidar97.htm

Charlson, R. J. (Ed.) Aerosol forcing of climate, J. Wiley, 416pp, New York, 1995.

d'Almeida, G., P Koepke, and E. P. Shettle, Atmospheric aerosols, 561 pp., A Deepack, Hampton, VA, 1991.

Gobbi, G. P., Parametrization of stratospheric aerosol physical properties on the basis of Nd-YAG lidar observations, Applied Optics, 37, 4712-4720, 1998.

Hinkley, E. D. (Ed.), Laser monitoring of the atmosphere, Springer Verlag, 380pp, New York, 1976.

Kerker, M., The scattering of light and other electromagnetic radiation, Acad. Press, New York, 1969

Klett, J. D., Lidar inversion with variable backscatter/extinction ratios, Applied Optics, 24, 1638-1643, 1985.

Kovalev, V. A., Lidar measurement of the vertical aerosol extinction profiles with range-dependent backscatter to extinction ratio, Applied Optics, 30, 6053-6065, 1993.

Liao, H., and J.H. Seinfeld, Radiative forcing by mineral dust aerosols: Sensitivity to key variables, J. Geophys. Res., 103, 31637-31645, 1998.

Measures, R. M., Laser Remote Sensing, J. Wiley, New York, 510 pp., 1984.

Mishchenko, M. I. et al., Modeling phase functions for dustlike tropospheric aerosols using a shape mixture of randomly oriented polydisperse spheroids, J. Geophys. Res., 102, 16,831-16,847, 1997.

Toon, O. B., E. V. Browell, S. Kinne and J. Jordan, An analysis of lidar observations of polar stratospheric clouds, Geophys. Res. Lett., 17, 393-396, 1990.

Young, A. T., Revised depolarization corrections for atmospheric extinction, Appl. Opt., 19, 3247-3248, 1980.

Lidar-related Web Sites:

LIDAR BIBLIOGRAPHY:	**http://www.osa.org/HOMES/GENERAL/BIBLIO/lidar97.htm**
LIDAR DIRECTORY:	**http://www-arb.larc.nasa.gov/lidar/directory.html**
Shuttle lidar LITE:	**http://www-arb.larc.nasa.gov/lite/**